Cell Reports
Physical Science

CellPress
OPEN ACCESS

Article

High safety and cycling stability of ultrahigh energy lithium ion batteries

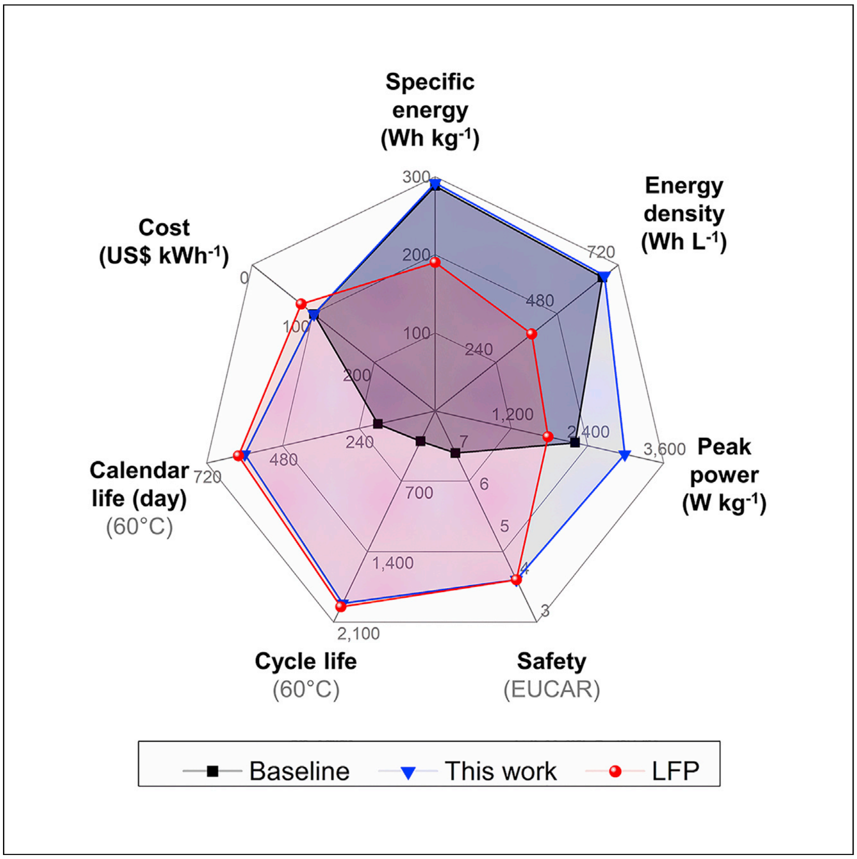

High-energy lithium-ion batteries for electric vehicles use cathode materials with poor thermal stability, introducing the threat of thermal runaway. Ge et al. present a facile interface passivation method to create a heat-resistant battery and prevent short-circuit-induced thermal runaway while providing high power, high energy, and long cycle life during operation at 60°C.

Shanhai Ge, Ryan Sheldon Longchamps, Teng Liu, Jie Liao, Yongjun Leng, Chao-Yang Wang

cxw31@psu.edu

Highlights

Interface passivation prevents thermal runaway of a 292-Wh kg^{-1} lithium-ion battery

Over 2,413 cycles were achieved with 76% capacity retention at 60°C

Power and energy are restored and improved with thermal modulation to ca. 60°C

Ge et al., Cell Reports Physical Science *2*, 100584
October 20, 2021 © 2021 The Authors.
https://doi.org/10.1016/j.xcrp.2021.100584

Please cite this article in press as: Ge et al., High safety and cycling stability of ultrahigh energy lithium ion batteries, Cell Reports Physical Science (2021), https://doi.org/10.1016/j.xcrp.2021.100584

Cell Reports
Physical Science

CellPress
OPEN ACCESS

Article

High safety and cycling stability of ultrahigh energy lithium ion batteries

Shanhai Ge,[1] Ryan Sheldon Longchamps,[1] Teng Liu,[1] Jie Liao,[1] Yongjun Leng,[1] and Chao-Yang Wang[1,2,*]

SUMMARY

High-nickel layered oxide Li-ion batteries (LIBs) dominate the electric vehicle market, but their potentially poor safety and thermal stability remain a public concern. Here, we show that an ultrahigh-energy LIB (292 Wh kg^{-1}) becomes intrinsically safer when a small amount of triallyl phosphate (TAP) is added to standard electrolytes. TAP passivates the electrode-electrolyte interfaces and limits the maximum cell temperature during nail penetration to 55°C versus complete cell destruction (>950°C) without TAP. The downside of this reliable safety solution is higher interfacial impedance and hence lower battery power; however, thermal modulation for battery operation around 60°C can restore power completely. When cycled at 60°C, the cell stabilized with TAP achieved 2,413 cycles at 76% capacity retention. Such an unconventional combination of interface-passivating electrolyte additive with cell thermal modulation renders the most energy-dense LIBs even safer than LiFePO$_4$ chemistry, while enjoying high power and cycling stability concurrently.

INTRODUCTION

As a growing number of governments have set time frames to phase out internal combustion engine vehicles (ICEVs) (https://theicct.org/blog/staff/global-ice-phaseout-nov2020), the era of electric vehicles (EVs) powered by lithium-ion batteries (LIBs) has reached apparent irreversibility, as further evidenced by the rapid growth of their market share (https://www.mckinsey.com/industries/automotive-and-assembly/our-insights/mckinsey-electric-vehicle-index-europe-cushions-a-global-plunge-in-ev-sales#), expansion of infrastructure (https://www.nrel.gov/docs/fy20osti/77508.pdf), governmental support (https://www.acea.auto/fact/overview-electric-vehicles-tax-benefits-purchase-incentives-in-the-european-union/), and commitment from automobile manufacturers (https://www.wsj.com/articles/gm-sets-2035-target-to-phase-out-gas-and-diesel-powered-vehicles-globally-11611850343). A key driver for the viability of this trend is the extension of EV range. In the past decade or so, discovery of high-voltage, high-capacity cathode materials like high-nickel ternary layered oxides $LiNi_{0.8}Co_{0.15}Al_{0.05}O_2$ (NCA) or $LiNi_{0.8}Co_{0.1}Mn_{0.1}O_2$ (NCM811)[1] has enabled an increase of cell-level energy density from ~150 Wh kg^{-1} to ~300 Wh kg^{-1}, which supports an ~400-mile (~644 km) range, nearing parity with that of ICEVs. As such, current long-range EVs often prefer NCM811 or NCA (e.g., BMW iX3 [https://pushevs.com/2020/07/15/bmw-ix3-gets-a-ncm-811-battery-from-catl/], Tesla Model 3 [https://www.evspecifications.com/en/news/49c5377], and Volkswagen MEB [https://pushevs.com/2020/09/28/catl-ncm-811-battery-cells-are-problematic/]), foregoing the much safer but less energy dense alternative LiFePO4 (LFP).[2–4]

---

[1] Department of Mechanical Engineering and Electrochemical Engine Center (ECEC), The Pennsylvania State University, University Park, PA 16802, USA

[2] Lead contact

*Correspondence: cxw31@psu.edu

https://doi.org/10.1016/j.xcrp.2021.100584

Please cite this article in press as: Ge et al., High safety and cycling stability of ultrahigh energy lithium ion batteries, Cell Reports Physical Science (2021), https://doi.org/10.1016/j.xcrp.2021.100584

Unfortunately, high-nickel cathodes possess poor thermal and chemical/electrochemical stability,[5–9] and when paired with flammable electrolytes, they are prone to violent thermal failure (i.e., thermal runaway), resulting in fire and explosion.[8,9] Although EVs are generally safer than ICEVs,[9] battery fires and explosions still receive intense public scrutiny and remain a major hurdle as the automotive industry quickens its shift to an electrified future.

Internal short circuit (ISC) is commonly recognized as the primary cause of fire accidents,[10,11] and nail penetration (NP) is a standard test to simulate the ISC condition and represents the most stringent safety test of LIBs. Because ternary-cathode-based cells cannot pass the NP test, some national standards have simply removed the NP qualification to accelerate the commercial introduction of these materials. In consequence, the safety issue persists, as seen in numerous highly publicized EV fires and/or explosions.[10] A recent report showed that 95% of EV safety incidents in China in 2019 were on EVs powered by ternary batteries and only 5% were on LFP batteries. Considering that 65.2% and 32.5% of passenger EVs use ternary and LFP cathodes, respectively,[12] ternary batteries are roughly 10 times more dangerous than LFP cells in the field.

Active material surface modification/coating by salt or solvent additives is a common approach for improving the performance of NCM cathode materials, but most studies focus on improving the electrochemical performance for a better cycle life at conventional or high cutoff voltages rather than improving the safety in the event of ISC.[13–17] In this work, we present a new and commercially viable strategy for an extremely safe, energy dense battery (SEB). The SEB strategy harnesses (1) *in situ* interface passivation by the additive triallyl phosphate (TAP) to guarantee a benign response to abuse conditions such as NP as well as long service life and (2) thermo-modulation before battery use to deliver high power and energy. We demonstrate that our 292-Wh kg^{-1} SEB cells with NCM811 as the cathode can limit cell temperature to 55°C during NP, which is well below flammability limits of LIB materials and even lower than the peak temperature of LFP cells (79°C) during NP, as measured by Sandia National Laboratories.[18] Rapidly elevating cell temperature to 60°C before battery use by a self-heating structure[19] then delivers on-demand power and high deliverable energy that exceed those of the baseline cell at room temperature (RT). Whether at rest at RT or in operation at high temperature, the stable electrode-electrolyte interfaces (EEIs) of the SEB enable long cycle/calendar life and suppress cell swelling/resistance growth to minimize power fade.

RESULTS

Intrinsic safety

To establish high specific energy ($\sim$290 Wh kg^{-1}; Tables S1 and S2) and energy density (658 Wh L^{-1}), we develop all cells with high areal capacity graphite anodes (4.58 mAh cm^{-2}) and NCM811 cathodes (4.04 mAh cm^{-2}). Baseline cells use a standard electrolyte (1 M $LiPF_6$ in ethylene carbonate [EC]/ethyl methyl carbonate [EMC] [3/7 wt] + 2 wt % vinylene carbonate [VC]). Two simple modifications are made in the SEB electrolyte to significantly improve safety:[20] (1) a reduction in EC content with an EC/EMC ratio of 1/9 by wt and (2) the addition of a small amount of TAP (0.5, 1.0, 1.5, and 2.0 wt % for SEB-1, -2, -3, and -4, respectively). The TAP is polymerized on the anode and cathode at a cell voltage of $\sim$2.73 V (Figure S1) to form a strong and resilient solid electrolyte interphase (SEI) layer and cathode electrolyte interphase (CEI) layer *in situ* during the initial charge/discharge cycle.[20–23]

Please cite this article in press as: Ge et al., High safety and cycling stability of ultrahigh energy lithium ion batteries, Cell Reports Physical Science (2021), https://doi.org/10.1016/j.xcrp.2021.100584

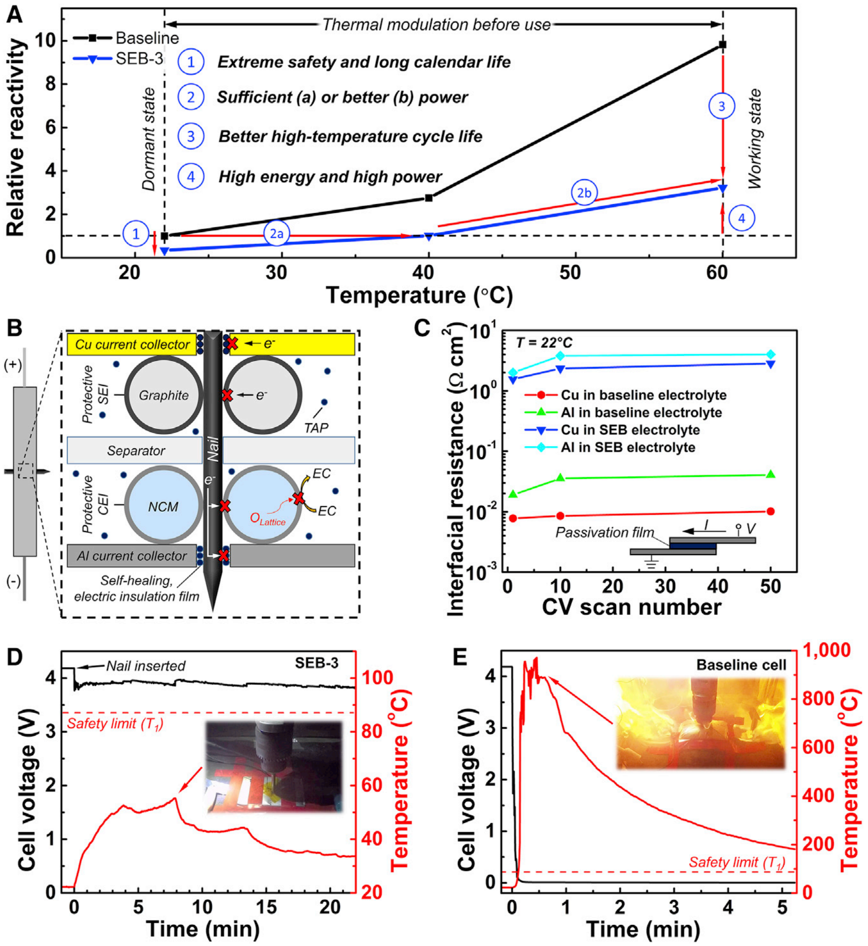

Figure 1. Extreme safety achieved with passivation and self-healing

(A) Relative reactivity, defined as $R_{ct,baseline@RT}/R_{ct}$, versus temperature for baseline and SEB-3 cells as obtained from electrochemical impedance spectroscopy (Figure S2). The robust passivation layers of the SEB reduce cell reactivity to provide extreme safety in the event of internal short circuit as well as long calendar life through the suppression of side reactions/self-discharge. Thermal modulation by rapid and efficient self-heating provides power on demand and augmented deliverable energy. At high temperatures, the stable EEIs continue to provide safety while ensuring long battery life.

(B) Schematic of SEB passivation layers that inhibit side reactions and provide protection and self-healing in the event of cell puncture. In a process analogous to platelet agglutination at an open wound in the human body, TAP diffuses to freshly exposed metallic surfaces to create an insulation film that hinders electron transport during internal short circuit. The thick protective layers on the surfaces of graphite and NCM particles also act as an electrical insulator.

(C) Interfacial resistance of copper and aluminum foils after cyclic voltammetry (CV) in different electrolytes. Each CV cycle takes only 1 min, indicating the rapid nature of the self-healing process.

(D and E) Cell voltage and temperature evolution during nail penetration of a SEB-3 and baseline cell, respectively. The baseline cell enters complete thermal runaway to temperatures nearing 1,000°C, whereas the SEB cell with TAP limits maximum cell temperature to only 55°C.

Relative to the baseline, the strongly passivated EEIs in an SEB cell yield a 3× reduction in reactivity (Figure 1A), as measured with electrochemical impedance spectroscopy (EIS; Figure S2). This reduces the cell discharge rate and hence the energy release and ensuing temperature rise during ISC, which is the underlying cause of thermal runaway in over 90% of cases.[11] In a process analogous to platelet agglutination at an open wound in the human body, TAP in the electrolyte also offers

Please cite this article in press as: Ge et al., High safety and cycling stability of ultrahigh energy lithium ion batteries, Cell Reports Physical Science (2021), https://doi.org/10.1016/j.xcrp.2021.100584

protection against ISC by quickly passivating any unintentional conductive pathways (e.g., penetration by metal object during vehicle crash) and blocking short circuit current, as illustrated in Figure 1B. To verify this mechanism, we measured the electronic interfacial resistance of bare current collectors passivated by each electrolyte. In the SEB electrolyte, high interfacial resistance evolves rapidly, and the resistance of both the aluminum and copper current collectors is at least two orders of magnitude higher than that of the baseline case (Figure 1C).

The net benefit to safety is assessed through NP testing of fresh cells beginning at RT, during which the SEB of 3.275 Ah displayed a maximum temperature of only 55°C (Figure 1D) with no signs of violent failure (Video S1) versus >950°C accompanied by smoke and fire in the baseline cell of equal capacity without the TAP additive (Figure 1E; Video S2). In comparison, NP of NCM cells from Sandia National Laboratories[18] and BYD (https://insideevs.com/news/406839/byd-blade-battery/) (peak temperatures of 549°C and >500°C, respectively) confirms the great danger of unprotected ternary LIBs. The temperature threshold for safety (T_1), which is the temperature at which the cell materials begin to exothermically decompose and initiate the process leading to thermal runaway, was characterized by accelerating rate calorimetry (ARC; Figure S3). For both the baseline and SEB cells, self-heating began at ~87°C (T_1) followed by thermal runaway initiation at ~181°C (T_2) and a maximum temperature of ~506°C (T_3); thus, the SEB avoided the threat of thermal runaway, remaining 32°C below T_1 during NP. To test the safety of SEB cells under harsher conditions, we also performed NP after heating the SEB to 60°C (Video S3). Even in a more reactive state, the SEB neither reached T_1 (Figure S4) nor triggered thermal runaway. In fact, the cell temperature decreased immediately upon NP, indicating that the stable EEIs and self-healing electrolyte additive between nail and current collectors effectively limited heat generation even when the SEB was initially at the elevated temperature. For perspective, the safest EV batteries based on LFP cathodes can restrict peak temperatures to 63°C, 79°C, 122°C, and 187°C during NP, avoiding violent thermal runaway as reported in references [2,3,4,18], respectively. In a commercial setting, the BYD blade battery with an LFP cathode is considered the safest EV battery on the market and can restrict peak cell temperature during NP to 60°C (https://insideevs.com/news/406839/byd-blade-battery/). The long, blade-like shape (~100-cm length) along with a rigid aluminum case provide a large thermal mass to reinforce its safety. Unfortunately, such safety in LFP-based cells comes at a sacrifice to energy density. In contrast, the SEB without a rigid casing/large thermal mass can provide a level of safety comparable to that LFP cells while simultaneously offering high energy density to satisfy range requirements in the evolving EV market.

The extreme safety of the SEB cell is also supported by the electrical behavior of the cell during NP. The voltage of the SEB cell drops from 4.183 V to 3.770 V in the first second after NP, then recovers to 3.912 V, and stabilizes within 5 s after penetration, evidencing a slow and controlled discharge ensured by the high shorting resistance and rapid self-healing mechanism (Figure S5). To quantify the short-circuit current in the nail, we use Ohm's law as follows:

$$i_{short} = \frac{V_{OCV} - V_{cell}}{R_{cell}} = \frac{V_{cell}}{R_{short}} = \frac{V_{OCV}}{R_{cell} + R_{short}} \qquad \text{(Equation 1)}$$

where V_{OCV} and V_{cell} are open circuit and cell voltages, respectively, and R_{cell} and R_{short} are the cell internal and short-circuit resistances, respectively. Based on the SEB cell resistance at RT and 100% state of charge (SOC) (54.45 mΩ; Table S3), the short circuit resistance, including contact resistances between the nail and current collectors, reached 786.07 mΩ, whereas the short-circuit current was limited

Please cite this article in press as: Ge et al., High safety and cycling stability of ultrahigh energy lithium ion batteries, Cell Reports Physical Science (2021), https://doi.org/10.1016/j.xcrp.2021.100584

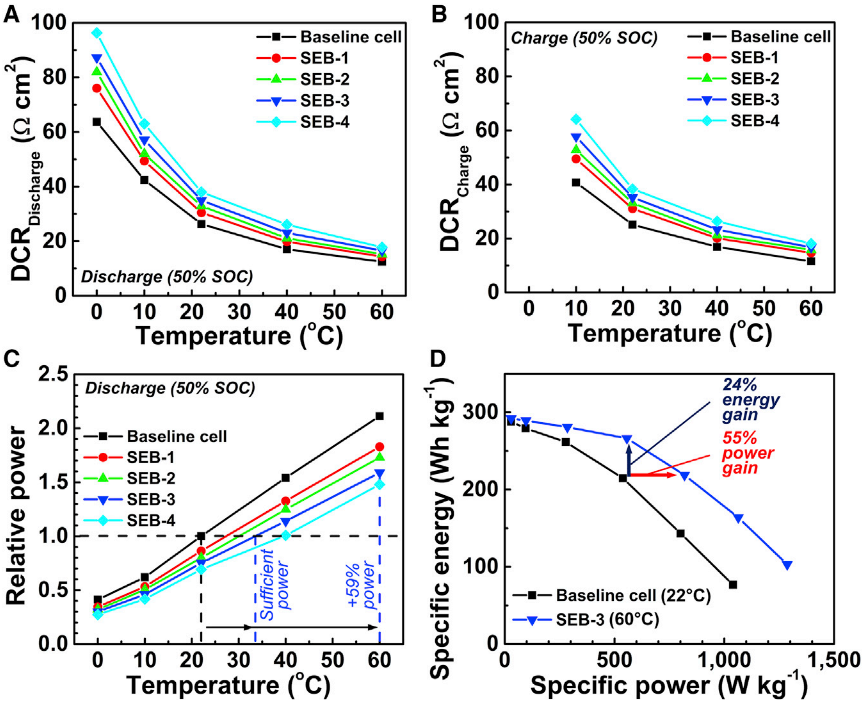

Figure 2. Temperature dependence of cell power performance

(A and B) Temperature dependence of direct current resistances (DCRs) of discharge and charge, respectively, at 50% state of charge for SEB cells versus the baseline LIB cell.

(C) Relative discharge power, defined as $DCR_{baseline@RT}/DCR$, of SEB cells versus the baseline LIB cell, showing that thermally modulated SEB cells operated at appropriate elevated temperatures, e.g., SEB-3 at 33.5°C, can deliver equal power to the baseline at the ambient temperature.

(D) Energy-power relationship of SEB-3 at 60°C and baseline cell at room temperature.

to only 6.135 mA cm^{-2} or 1.52C in C-rate (Table S4). When penetrated at 60°C, the SEB voltage dropped to 4.063 V, implying a short-circuit current of 5.324 mA cm^{-2} or 1.32C. In the baseline cell that immediately entered thermal runaway, the cell voltage dropped from 4.187 V to 0.109 V within 5 s after penetration, which corresponds to a short circuit resistance of only 0.89 mΩ and a short circuit current of 151.1 mA cm^{-2} or ~37C. The lack of voltage recovery in the baseline case indicates that TAP is responsible for this effect in the SEB cell. Thus, in the event of an ISC caused by penetration by a metal object, stray conductive particles inside the cell, or lithium dendrites that penetrate the separator, all of which are covered by an electrically insulating film due to presence of TAP, the SEB can provide a ~95% reduction in short circuit current at any operating temperature—the key to ensuring passenger safety in long-range EVs.

It is noteworthy that a small amount of TAP additive (1–2 wt %) can effectively passivate EEIs and largely restrict energy release during internal shorting for absolute safety. In practice, such a solution appears to be superior to using flame-retardant electrolytes, fire-extinguishing additives, or phase change materials for heat absorption, of which all require a substantial amount of mass (several-fold of battery mass) to absorb all electrical energy released from a LIB, as estimated from a simple thermodynamic analysis.

Power and energy restored through thermal modulation

Although the addition of TAP greatly enhances battery safety, the strongly passivated EEIs inevitably impede power generation. This is shown in Figures 2A and 2B in the form of direct current resistance (DCR) measured with hybrid pulse power characterization (HPPC). However, temperature modulation and battery operation at elevated temperatures can readily restore power to practical levels, representing the second key component in the SEB concept. For example, heating SEB-3 from RT to 33.5°C achieves parity with the power performance of the baseline at RT (Figure 2C), and further heating to 60°C provides 59% more power over the baseline at RT, reaching high power levels designed for plug-in hybrid EV applications. Therefore, power performance is not sacrificed for safety but rather increased in the SEB. Moreover, at low ambient temperatures (T_{amb}s) such as 0°C, the baseline cell relative power drops to 0.41, whereas the thermally modulated SEB-3 operated at 60°C maintains a relative power of 1.59, representing a ~4× boost in power when working in freezing environments.

The practicality of power on demand hinges on rapid and energy-efficient cell heating. This requirement is satisfied by the self-heating cell architecture reported earlier,[19] which briefly discharges the cell energy through a μm-thick, internal nickel foil(s) stacked with the electrode layers to create substantial heat and uniformly warm the cell at rates of 1°C s^{-1}–2°C s^{-1}. The SEB cells have a specific heat of ~860 J kg^{-1} $°C^{-1}$ or 0.239 Wh kg^{-1} $°C^{-1}$ (Table S2) and a nominal specific energy of 292 Wh kg^{-1}, meaning that heating energy consumption is only 0.082% $°C^{-1}$. Thus, heating the SEB from 22°C to 60°C consumes only 3.1% of cell energy and takes 19–38 s in situations in which peak power is demanded instantaneously. In cases in which sub-peak power is needed, the SEB can be operated from the T_{amb} with natural warmup and no forced self-heating, i.e., consuming zero electrical energy.

Beyond power on demand, the SEB also provides an increase in usable energy (Figure S6). All electrochemical energy storage systems suffer a loss of deliverable energy with increasing power (Figures 2D and S7). However, thermally modulating the SEB to 60°C shifts the trend upward, reducing the severity of this inherent dilemma. For example, the SEB provides a 24% boost in deliverable energy at ~500 W kg^{-1} operation (2C discharge), which represents high sustained power for EV batteries.[24] High power and energy achieved in a single-cell design indicate that an EV powered by SEB technology can deliver long range regardless of the power demands during the drive cycle. Furthermore, the benefit to energy is not completely sacrificed for cell heating. Considering the 3.1% heating energy required to reach 60°C, SEB-3 could still deliver 11.35 Wh of its total 11.71 Wh at 60°C and 1C rate as compared to the 11.01 Wh of the baseline cell at RT and the same rate (see Figure S6B). Thus, the SEB energy after pre-heating is still ~3% greater than that of the energy-dense baseline.

High stability and long service life

To be cost-effective and considerate of limited material resources, batteries must have a long cycle/calendar life. Battery degradation is highly temperature dependent, and elevated temperatures accelerate EEI layer growth and gas evolution, which both reduce cell capacity, increase resistance, and cause swelling. Such side reactions/effects are detrimental to EV performance and give rise to safety concerns.[25,26] For LIBs using traditional electrolytes that form thin EEIs with low thermal stability, cycling at an elevated temperature of 60°C leads to significant capacity fade from material fracture and Li consumption by side reactions. In contrast, the SEB exhibits robust high-temperature cycling performance. At 80% capacity retention, the baseline cell achieved only 303 cycles at 60°C and 1,706 cycles at RT (Figures 3A and S8), and a large reduction in coulombic efficiency was observed in the late stages (Figure S9B). In comparison, SEB-3 performed 1,914 cycles at 60°C before reaching 80% capacity retention, representing a 6.3× and 1.1× increase,

Please cite this article in press as: Ge et al., High safety and cycling stability of ultrahigh energy lithium ion batteries, Cell Reports Physical Science (2021), https://doi.org/10.1016/j.xcrp.2021.100584

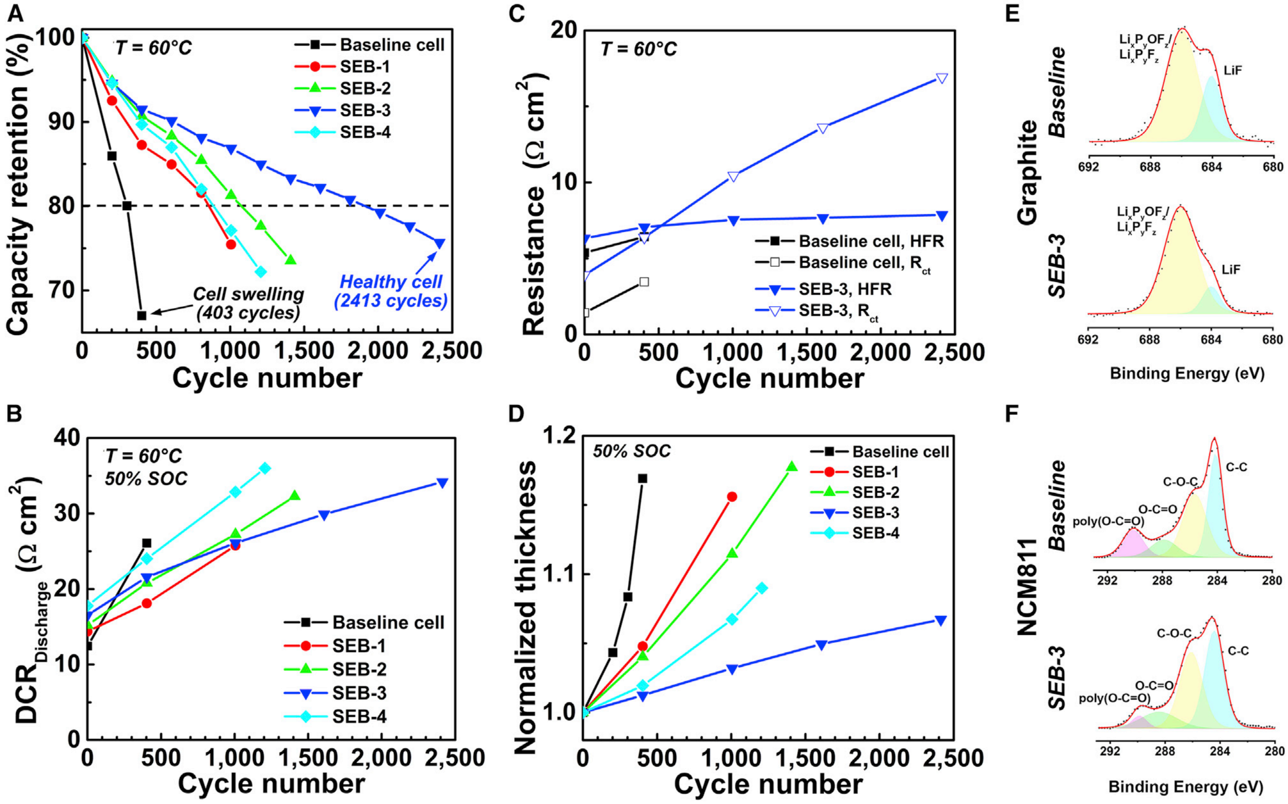

Figure 3. High-temperature cycling stability

(A–D) For cycling of SEB and baseline cells at 60°C; capacity retention (A), DCR (B), high-frequency and charge transfer resistances (C), and normalized cell thickness (D). The robust EEIs in the SEB-3 significantly extend cycle life over the baseline while reducing gas evolution, cell swelling, and resistance increase.

(E and F) F 1 s and C 1 s XPS spectra for fresh and aged baseline (403 cycles) and SEB-3 (2,413 cycles) cells, verifying the presence of the advantageous SEB EEIs as compared to the baseline. Additional XPS results are presented in Figure S10.

respectively. Moreover, SEB-3 underwent 2,413 cycles with only 24% capacity loss and showed no signs of impending cell failure, such as a rapid drop in capacity or visible cell swelling/deformation. The average discharge capacity of these 2,413 cycles is 85.8% of an equivalent full cycle. Assuming a 644-km (400-mile) driving range for an EV equipped with a 100-kWh battery pack (e.g., 2021 Tesla model S), 2,413 cycles corresponds to ~1,333,000 km (828,000 miles) of lifetime.

As suggested, minimization of resistance growth and suppression of cell swelling underlie this dramatic extension of cycle life. In the case of SEB cells, the DCR of the fresh cell is initially larger than that of the baseline cell by design; however, its rate of increase is much slower due to the strongly stabilized coatings on both the graphite and NCM811 particles (Figures 1A and 3B). Moreover, the charge transfer resistance increases much faster than the high-frequency resistance for both the baseline and SEB cells, indicating that the resistance at the interfaces dominates the DCR increase and in consequence capacity and power fade (Figures 3C and S10). As for cell swelling, the baseline cell swelled 16.9% in thickness after 403 cycles, whereas the SEB-3 cell expanded only 6.7% after 2,413 cycles, indicating that the expansion rate of the baseline cell is ~15× that of the SEB-3 cell (Figure 3D).

To investigate EEI dependence on TAP, we conducted X-ray photoelectron spectroscopy (XPS) on the SEB-3 and baseline electrodes after 2,413 and 403 cycles, respectively (Figures 3E, 3F, and S11). For the graphite anodes, the SEB-3 SEI has much higher C and P contents than the baseline cell (Figure S12). The detailed peaks show that the baseline sample has more LiF (F 1 s, 684.5 eV), O-C = O (C 1 s, 288.8 eV), and poly(O-C = O) (C 1 s, 290.1 eV), which are the decomposition products of organic solvents.[27] In comparison, more $Li_xP_yF_z/Li_xP_yOF_z$ (F 1 s, 686.9 eV), C-C (C 1 s, 284.6 eV), and C-O (C 1 s, 286.1 eV) are found in the SEB-3 SEI, suggesting the decomposition of TAP on the anode. This finding agrees with previous reports that the decomposition products of TAP are richer in $Li_xP_yF_z/Li_xP_yOF_z$ species.[21] On the cathode, the CEI contains considerably higher contents of P and O for SEB-3, which is also due to the decomposition of TAP. The much weaker peak corresponding to poly(O-C = O) (C 1 s, 290.1 eV) in the SEB-3 CEI suggests that TAP suppresses the oxidative decomposition of the organic solvents on the cathode (Figure 3F). It is also found that the peak corresponding to lattice O_2^- (O 1 s, 529.2 eV) is much weaker with the addition of TAP, which suggests that the CEI formed on the SEB-3 cathode is much thicker than that of the baseline cathode and is consistent with previous reports by Dahn's group for a coated NCM424 surface[21] and our group for a coated NCM622 surface,[20] both in the presence of TAP additive.

We also performed scanning electron microscopy (SEM) on the electrodes of both cells (Figure S13). The expansion of the graphite anode during cycling squeezes out some graphite particles in both aged baseline and SEB-3 cells as opposed to the smoother surface in the fresh anodes. On the cathode, the high-nickel NCM particles are prone to micro-cracks along grain boundaries,[28–30] leading to more severe electrolyte oxidation[31] and rock salt formation,[32] as well as potential electronic isolation of active material.[33] For both cells, the aged cathodes present similar yet minor levels of cracking around the perimeter of the particles, indicating that the SEB withstood 6× more cycling before reaching a similar level of degradation to the baseline. Differential capacity analysis confirms the similarity of degradation from a bulk electrode perspective (Figure S14). From the XPS, SEM, and differential capacity analysis results, we confirm that TAP plays an important role in the formation of thick and protective EEIs on the electrodes.

EV batteries spend a significant portion of their lifetime at rest (90%–95%), and degradation persists even in this state, the significance of which increases in systems with highly reactive materials such as NCM811. We conducted constant voltage storage tests at both RT and 60°C for the baseline and SEB-3 cells at 100% SOC to assess calendar aging. For all four cases, the self-discharge current decreases as the EEIs develop and stabilize, but the fresh SEB cells show self-discharging currents 6× and 7× lower than those of the baseline at RT and 60°C, respectively (Figure 4A). After 20 days of storage, the self-discharge currents begin to plateau. Beyond this point, the SEB in the dormant state (RT) is 3× lower than that of the baseline on average. Even in the active state (60°C), the SEB self-discharge rate is comparable to that of the baseline at RT, albeit it is slightly higher. Thus, regardless of the SEB thermally activated state, the protective EEIs achieve a calendar life similar to or better than the baseline at RT. The calendar aging test also shows that the SEB cell does not generate gas at either RT or 60°C as opposed to ~1.4 mL generated by the baseline in only 20 days at 60°C (Figure 4B). Moreover, a loss of vacuum pressure and substantial swelling was apparent in the baseline cell at high temperature within only 7 days. The suppression of cell swelling from EEI growth and/or gas evolution in the SEB is evidenced by the dramatic slowing of cell thickness evolution (Figure 4C). The net effect is an overall extension of calendar life, which is quantitatively represented by capacity retention in Figure 4D where, again, the SEB demonstrates equivalent or slower calendar aging at 60°C and RT, respectively, than that of the baseline at RT.

Please cite this article in press as: Ge et al., High safety and cycling stability of ultrahigh energy lithium ion batteries, Cell Reports Physical Science (2021), https://doi.org/10.1016/j.xcrp.2021.100584

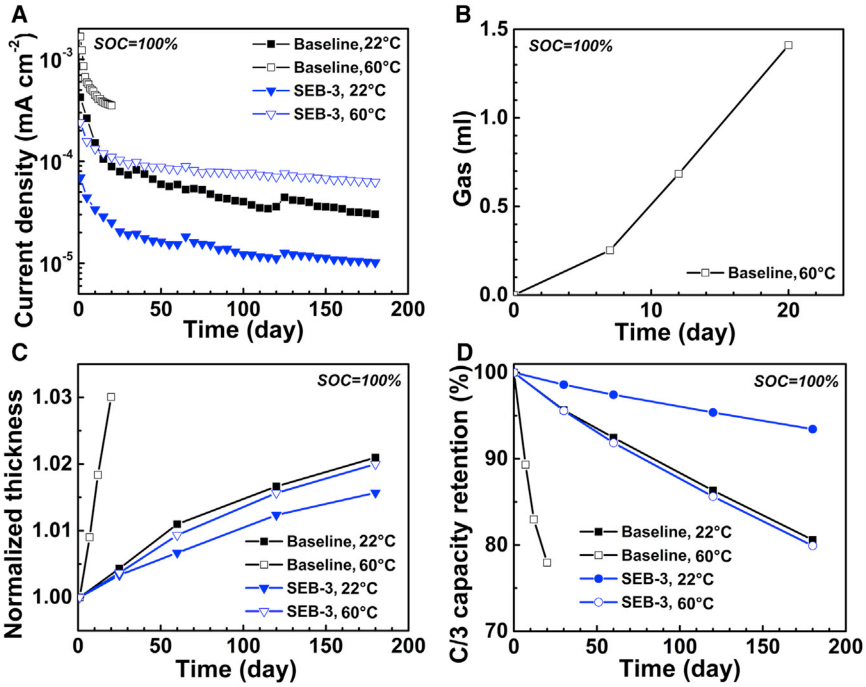

Figure 4. Calendar aging performance

(A) Self-discharge current density at 22°C and 60°C for the baseline and SEB-3 cells.

(B) Gas volume evolution for the baseline cell produced during calendar aging at 60°C.

(C and D) Cell thickness and C/3 capacity retention of the baseline and SEB-3 cells during calendar aging at 22°C and 60°C.

In the previous discussion of cycle life, we focused on the advantages of SEB-3 with 1.5 wt % TAP. With regard to electrolyte optimization, the results show that incrementally increasing TAP content up to 1.5 wt % provides benefits to cycle life in a monotonic fashion (Figure 3). When 2 wt % TAP was introduced, the performance regressed; therefore, we conclude that an optimal SEB electrolyte formula consists of ~1.5 wt % TAP. We also investigated the effect of EC content on cycle life at 60°C for cells containing 0 wt %, 10 wt %, and 30 wt % EC with 1.5 wt % TAP in each case and found that EC content is optimal at ca. 10 wt % (Figure S15). Lastly, a 60°C cycle aging test of a cell with 1 M $LiPF_6$ in EC/EMC (1/9 wt) + 2% VC without TAP shows a marginal (12.2%) reduction in cycle life relative to the baseline electrolyte case (Figure S16), indicating that the addition of TAP is largely responsible for the high-temperature stability of the SEB. With the near-optimal electrolyte formula of SEB-3, we have shown that stable, long-term, and high-temperature operation of energy-dense cells is possible even when normally unstable NCM811 is used.[34]

DISCUSSION

In addition to the primary benefit to battery safety, the SEB offers cost, weight, and power savings for the battery thermal management system (BTMS) through a reduction in cooling requirements, which permits BTMS simplification or even elimination. Assuming an T_{amb} of 25°C and operation of the SEB-3 and baseline cells at 60°C and 30°C, respectively, the SEB cell provides a heat dissipation rate ($h(T_{\mathrm{cell}} - T_{\mathrm{amb}})$) 7× larger than that of the baseline case. Moreover, the internal resistance of the SEB-3 cell at 60°C (16.5 Ω cm^2) is lower than that of the baseline cell at 30°C (22.2 Ω cm^2), indicating that the heat generation rate (I^2R_{cell}) of SEB-3 at 60°C is 1.35× less than that of the baseline cell at 30°C. In balancing heat generation and dissipation, the

Please cite this article in press as: Ge et al., High safety and cycling stability of ultrahigh energy lithium ion batteries, Cell Reports Physical Science (2021), https://doi.org/10.1016/j.xcrp.2021.100584

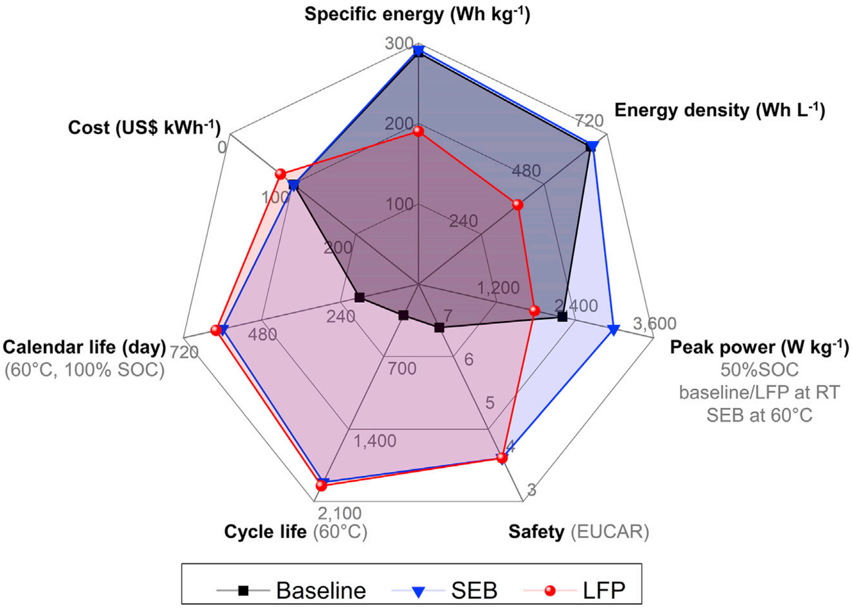

Figure 5. Satisfying performance and safety metrics with a single cell

Radar chart comparing the safety (European Council for Automotive R&D, EUCAR), specific energy, energy density, power density, cycle life, calendar life, and cost between SEB and baseline cells. Performance of state-of-the-art LFP cells is also presented as a reference. The SEB possesses the high performance of ternary cathodes as well as the safety and stability of LFP cathodes.

heat transfer coefficient (*h)* required for a SEB BTMS is reduced to one-ninth of that for a baseline battery pack. In this case, conventional active liquid cooling can be replaced with passive air cooling, which is much simpler, less costly, lighter, occupies less volume, and does not require parasitic pumping power.

With regard to material cost, TAP has a similar price as current standard solvents; thus, the addition of 1.5 wt % TAP will not significantly affect LIB cost. Moreover, the SEB electrolyte does not increase viscosity or reduce ion mobility/conductivity relative to conventional electrolytes, unlike many promising for next-generation batteries, such as high concentration,[35] ionic liquid,[36] or solid-state[37,38] electrolytes. In addition, NCM811 contains only 6 wt % cobalt, which is costly and resource limited, and thus cuts the price gap between NCM811 and LFP cells to ~25% and aids LIB sustainability. The slight cost disadvantage of NCM811 can be justified by the 53% and 69% increase in specific energy and energy density, respectively, when NCM811 is chosen over LFP (Table S1). Figure 5 summarizes the cost and performance of the baseline and SEB-3 cells in this work along with LFP-based LIBs. The overlap of SEB traits with the best of the other two clearly illustrates the defiance of the many dilemmas that plague the traditional NCM811 and LFP cells. Overall, the SEB exhibits an alternative approach to ensure battery safety while simultaneously achieving high energy and power for EVs and more stringent applications (e.g., military, aeronautics, and space exploration).

More broadly, the proposed strategy of building robust interfacial layers for safety/long life and elevating operating temperature for high performance has profound implications for the future direction of battery materials development. Similar to high-nickel NCM, promising next-generation materials (e.g., Li metal,[39–41] silicon based,[42] Li rich,[43,44] or $LiNi_{0.5}Mn_{1.5}O_4$[45]) often sacrifice stability for high energy and/or power. Interfacial passivation with analogous methods can lend stability and safety to these inherently reactive materials while thermal modulation restores battery power in use.

EXPERIMENTAL PROCEDURES

Resource availability

Lead contact

Further information and requests for resources should be directed to and will be fulfilled by the Lead Contact, Chao-Yang Wang (cxw31@psu.edu).

Materials availability

This study did not generate new unique reagents.

Data and code availability

All data are available upon request without restriction.

Cell design and fabrication

We fabricated 3.275-Ah pouch cells using $LiNi_{0.8}Co_{0.1}Mn_{0.1}O_2$ for cathodes and graphite for anodes. The capacity ratio of the negative to positive electrode, or NP ratio, is 1.13. The 3.275-Ah pouch cell contains a stack of 11 anode and 10 cathode layers. A Celgard-2325 separator of 25 μm in thickness is used. The loadings of NCM811 on the positive electrode and graphite on the negative electrode were 20.81 and 13.09 mg cm^{-2}, respectively.

The cathodes were prepared by coating a NMP-based slurry onto 13-μm-thick Al foil, whose dry material consists of NCM811 (97.7 wt %), Super-P (1.0 wt %), and polyvinylidene fluoride (1.3 wt %) as a binder. The anodes are prepared by coating a deionized-water-based slurry onto a 8-μm-thick Cu foil, whose dry material consists of graphite (97.7 wt %), styrene-butadiene rubber (1.3 wt %) and carboxymethyl cellulose (1.0 wt %). A total of 1 M $LiPF_6$ dissolved in EC/EMC (3/7 wt) + 2 wt % VC is used as the baseline electrolyte (Soulbrain, MI). To build SEB cells, 0.5–2.0 wt % TAP was mixed into the EC/EMC (1/9 wt) + 2 wt % VC electrolyte as an additive. A total of 6.97 g of electrolyte was used in all cells, regardless of electrolyte type.

Each experimental pouch cell has a 110 × 56 mm footprint area, weighs 48.7 g, and has 3.275-Ah nominal capacity with specific energy of 249 Wh kg^{-1} and energy density of 449 Wh L^{-1}. All the cells were initially cycled at RT and C/10 for 3 cycles and had a capacity of 3.275 $\pm$ 0.010 Ah. Discharge performance of the pristine baseline and SEB cells at RT is shown in Figure S7 as a function of C-rate.

Cycle aging tests

Cycle aging tests of the pouch cells were performed using the Land instrument battery testing system (model CT2001B; Land Instruments). A forced-air oven was used to control the ambient temperature. For each aging cycle, the cell was charged to 4.2 V at a constant current of 1.637 A (0.5 C-rate) and then charged at a constant voltage of 4.2 V until the current decreased to 0.164 A (C/20). After resting for 5 min, the cell was discharged to 2.8 V at constant current of 3.275 A (1 C-rate) followed by a final rest period of 5 min. When the cycle number reached a specific value (e.g., 403, 1,006 cycles), reference performance tests were performed by cycling at a charge and discharge rate of C/3 to characterize the capacity of the cell.

Resistance and thickness characterization

For impedance tests at different temperatures, the cells were fully charged and then discharged at a rate of C/3 to 90% SOC. Electrochemical impedance spectroscopy

Please cite this article in press as: Ge et al., High safety and cycling stability of ultrahigh energy lithium ion batteries, Cell Reports Physical Science (2021), https://doi.org/10.1016/j.xcrp.2021.100584

(EIS) was performed with an AC voltage amplitude of 5 mV in the frequency range of 50 kHz to 0.01 Hz. For DCR tests, the cells were fully charged and then discharged to 50% SOC at C/3-rate, and then hybrid pulse power characterization (HPPC) was performed at the characterization temperature. HPPC consisted of a 10-s discharge at 5C, a 40-s rest, and a 10-s charge at 3.75C. The $DCR_{Discharge}$ and DCR_{Charge} were determined with Equation 2 where V_{10s} was the cell voltage at the end of the respective discharge (or charge) pulse. For thickness measurement, cell thickness was measured at 10 positions by using a micrometer (Mitutoyo) and then averaged.

$$DCR_i = \left| \frac{V_{OCV} - V_{10s}}{i_i} \right| \qquad \text{(Equation 2)}$$

Calendar aging tests

Calendar aging tests were performed at different ambient temperatures in a forced-air oven. By use of the Land system, the cell voltage was held constant and the current was measured. When the calendar aging time reached a specific value (e.g., 30, 60, 120, and 180 days), the cell was cycled at a charge and discharge rate of C/3 to determine the capacity of the cell. Then impedance and DCR tests were conducted under the same conditions as those for the cycle-aged cells. The volume of gas generated by the baseline cell was measured using the Archimedes principle. Cells were first weighed in air and then weighed while submerged in water to obtain the volume of water displaced and thus the cell volume.

Interfacial resistance characterization

For electronic interfacial resistance tests, copper or aluminum foil was soaked in the baseline or SEB-3 electrolyte. Cu (or Al) was set as the working electrode, and Li foil was set as the counter and reference electrodes. Cyclic voltammetry was used to passivate the current collector samples. Scan windows for Cu and Al were 0.05–1.6 V and 2.7–4.3 V, respectively. Scan rate was set as 50 mV s^{-1}. After being scanned for 1, 10, and 50 cycles, the samples were extracted and washed with EMC three times. Two pieces of passivated foil were overlapped partially and clamped under a pressure of 0.3 MPa for each case. The overlapping area was 1 cm^2. Resistance was determined by applying a constant current while measuring voltage.

Nail penetration

For nail penetration tests, each cell was fully charged (0.3 C CCCV charge with cut-off voltage of 4.2 V and cut-off current of C/20), and all cells had the same construction (i.e., same capacity) as the baseline experimental cell in Table S1. Two thermocouples were placed at 5 mm away from the geometric center of the cell, with one on either side. The nail diameter was 5 mm and was made of heat-resistant steel (point angle of the nail was 60°; nail surface was clean, free of rust or oil). The rate of penetration was 30 mm s^{-1}. The nail was driven through the geometric center of the cell, perpendicular to the electrode plane, and remained inside the cell. For RT NP tests of the baseline and SEB cells, NP was performed directly. In the high-temperature test of the SEB, an external heater was mounted to the bottom of the cell, and the cell temperature was slowly elevated to 60°C. Heating was stopped when the nail penetrated the cell to simulate the cooling effect in a battery pack with a thermal management system. Note only natural convection cooling was present during all NP tests.

Accelerating rate calorimetry

For accelerating rate calorimetry (ARC), the EV-ARC (Thermal Hazards Technology) was used in the standard heat-wait-seek mode. The ARC test was started at 40°C, after which the fully charged cell was heated in 5°C increments (heat step). After each heating step, a wait time of 20 min was applied for thermal equilibration prior to checking for self-heating based on a standard temperature rate sensitivity of 0.02°C min^{-1}. The ARC thermocouple was placed on the cell surface at the geometric cell center, and all electrical connections were isolated using polyimide tape.

SEM and XPS procedures

The SEM imaging and XPS analyses were performed by first extracting the electrode samples from the fully discharged graphite/NCM811 pouch cells after cycling and washing with EMC three times. XPS tests were conducted on a PHI VersaProbe II scanning XPS microprobe. The samples were loaded in a glovebox and transferred into the instrument through a vacuum transfer vessel. The CasaXPS software was used to process XPS data. First, we calibrated binding using the C1s peak from C-C at 284.3 eV. Then, we fitted the core peaks with a U 2 Tougaard-type background and optimized the peak position/areas using 70% Gaussian-30% Lorentzian Voigt peak shapes and fullwidth at half-maximum (fwhm) constraint ranges. SEM imaging was performed on an FEI Nova NanoSEM 630 SEM instrument.

SUPPLEMENTAL INFORMATION

Supplemental information can be found online at https://doi.org/10.1016/j.xcrp.2021.100584.

ACKNOWLEDGMENTS

This work was partially supported by U.S. Department of Energy's Office of Energy Efficiency and Renewable Energy (EERE) under award number DE-EE0008447 and the William E. Diefenderfer Endowment.

AUTHOR CONTRIBUTIONS

S.G. and C.-Y.W. developed the concept. S.G., R.S.L., and C.-Y.W. wrote the manuscript. S.G. designed and built the cells and carried out the performance characterization. R.S.L. conducted the ARC tests. J.L. performed the SEM and XPS tests. T.L. carried out the nail penetration tests. Y.L. analyzed the impedance. All authors contributed to development of the manuscript and to discussions as the project developed.

DECLARATION OF INTERESTS

The authors declare no competing interests.

Received: May 23, 2021
Revised: August 2, 2021
Accepted: August 27, 2021
Published: September 20, 2021

REFERENCES

1. Julien, C.M., and Mauger, A. (2020). NCA, NCM811, and the route to Ni-richer lithium-ion batteries. Energies *13*, 6363.
2. Yamano, A., Morishita, M., Park, G., Sakamoto, T., Yamauchi, H., Nagakane, T., Ohji, M., Sakamoto, A., and Sakai, T. (2014). Development of high-capacity Li-ion batteries using phosphate-based materials and their safety evaluation. J. Electrochem. Soc. *161*, A1094–A1099.
3. Perea, A., Paolella, A., Dubé, J., Champagne, D., Mauger, A., and Zaghib, K. (2018). State of charge influence on thermal reactions and abuse tests in commercial lithium-ion cells. J. Power Sources *399*, 392–397.
4. Huang, Z., Li, H., Mei, W., Zhao, C., Sun, J., and Wang, Q. (2020). Thermal runaway behavior of lithium iron phosphate battery during penetration. Fire Technol. *56*, 2405–2426.
5. Bak, S.-M., Hu, E., Zhou, Y., Yu, X., Senanayake, S.D., Cho, S.-J., Kim, K.-B., Chung, K.Y., Yang, X.-Q., and Nam, K.-W. (2014). Structural changes and thermal stability of charged LiNixMnyCozO$_2$ cathode materials studied by combined in situ time-resolved XRD and mass spectroscopy. ACS Appl. Mater. Interfaces *6*, 22594–22601.
6. Manthiram, A., Song, B., and Li, W. (2017). A perspective on nickel-rich layered oxide cathodes for lithium-ion batteries. Energy Storage Mater. *6*, 125–139.
7. Ma, L., Nie, M., Xia, J., and Dahn, J.R. (2016). A systematic study on the reactivity of different grades of charged Li[Ni$_x$Mn$_y$Co$_z$]O$_2$ with electrolyte at elevated temperatures using

Please cite this article in press as: Ge et al., High safety and cycling stability of ultrahigh energy lithium ion batteries, Cell Reports Physical Science (2021), https://doi.org/10.1016/j.xcrp.2021.100584

accelerating rate calorimetry. J. Power Sources *327*, 145–150.

8. Wang, D., Zheng, L., Li, X., Du, G., Feng, Y., Jia, L., and Dai, Z. (2020). Effect of high Ni on battery thermal safety. Int. J. Energy Res. *44*, 12158–12168.
9. Huang, W., Feng, X., Han, X., Zhang, W., and Jiang, F. (2021). Questions and answers relating to lithium-ion battery safety issues. Cell Reports Phys. Sci. *2*, 100285.
10. Xiong, R., Ma, S., Li, H., Sun, F., and Li, J. (2020). Toward a safer battery management system: a critical review on diagnosis and prognosis of battery short circuit. iScience *23*, 101010.
11. Feng, X., Ren, D., He, X., and Ouyang, M. (2020). Mitigating thermal runaway of lithium-ion batteries. Joule *4*, 743–770.
12. Wang, C., Li, Y., and Liu, P. (2019). New Energy Vehicles Safety Monitoring Results Report. In China New Energy Vehicle Big Data Research Report (Social Sciences Academic Press (China).
13. Li, J., Wang, J., Lu, X., Jiang, H., Zhang, Q., Wang, B., and Lai, C. (2021). Enhancing high-potential stability of Ni-rich $LiNi_{0.8}Co_{0.1}Mn_{0.1}O_2$ cathode with PrF_3 coating. Ceram. Int. *47*, 6341–6351.
14. Tan, X., Zhang, M., Li, J., Zhang, D., Yan, Y., and Li, Z. (2020). Recent progress in coatings and methods of Ni-rich $LiNi_{0.8}Co_{0.1}Mn_{0.1}O_2$ cathode materials: A short review. Ceram. Int. *46*, 21888–21901.
15. Wang, C., Ouyang, L., Fan, W., Liu, J., Yang, L., Yu, L., and Zhu, M. (2019). Citraconic anhydride as an electrolyte additive to improve the high temperature performance of $LiNi_{0.6}Co_{0.2}Mn_{0.2}O_2$/graphite pouch batteries. J. Alloys Compd. *805*, 757–766.
16. Wang, C., Yu, L., Fan, W., Liu, R., Liu, J., Ouyang, L., Yang, L., and Zhu, M. (2018). Enhanced high-voltage cyclability of $LiNi_{0.5}Co_{0.2}Mn_{0.3}O_2$-based pouch cells via lithium difluorophosphate introducing as electrolyte additive. J. Alloys Compd. *755*, 1–9.
17. Wang, C., Yu, L., Fan, W., Liu, J., Ouyang, L., Yang, L., and Zhu, M. (2017). 3,3′-(Ethylenedioxy)dipropiononitrile as an electrolyte additive for 4.5 V $LiNi_{1/3}Co_{1/3}Mn_{1/3}O_2$/graphite cells. ACS Appl. Mater. Interfaces *9*, 9630–9639.
18. Lamb, J., Torres-Castro, L., Stanley, J., Grosso, C., and Gray, L. (2020). Evaluation of multi-cell failure propagation, SAND-2020-2802 (Sandia National Laboratories).
19. Wang, C.-Y., Zhang, G., Ge, S., Xu, T., Ji, Y., Yang, X.-G., and Leng, Y. (2016). Lithium-ion battery structure that self-heats at low temperatures. Nature *529*, 515–518.
20. Ge, S., Leng, Y., Liu, T., Longchamps, R.S., Yang, X.-G., Gao, Y., Wang, D., Wang, D., and Wang, C.-Y. (2020). A new approach to both high safety and high performance of lithium-ion batteries. Sci. Adv. *6*, eaay7633.
21. Xia, J., Madec, L., Ma, L., Ellis, L.D., Qiu, W., Nelson, K.J., Lu, Z., and Dahn, J.R. (2015). Study of triallyl phosphate as an electrolyte additive for high voltage lithium-ion cells. J. Power Sources *295*, 203–211.
22. Xu, K. (2014). Electrolytes and interphases in Li-ion batteries and beyond. Chem. Rev. *114*, 11503–11618.
23. Wang, L., Menakath, A., Han, F., Wang, Y., Zavalij, P.Y., Gaskell, K.J., Borodin, O., Iuga, D., Brown, S.P., Wang, C., et al. (2019). Identifying the components of the solid-electrolyte interphase in Li-ion batteries. Nat. Chem. *11*, 789–796.
24. Christophersen, J.P. (2015). Battery test manual for electric vehicles, revision 3 (US Department of Energy).
25. Willenberg, L.K., Dechent, P., Fuchs, G., Sauer, D.U., and Figgemeier, E. (2020). High-precision monitoring of volume change of commercial lithium-ion batteries by using strain gauges. Sustainability *12*, 557.
26. Müller, V., Scurtu, R.-G., Richter, K., Waldmann, T., Memm, M., Danzer, M.A., and Wohlfahrt-Mehrens, M. (2019). Effects of mechanical compression on the aging and the expansion behavior of Si/C-composite|NMC811 in different lithium-ion battery cell formats. J. Electrochem. Soc. *166*, A3796–A3805.
27. Gao, Y., Yan, Z., Gray, J.L., He, X., Wang, D., Chen, T., Huang, Q., Li, Y.C., Wang, H., Kim, S.H., et al. (2019). Polymer-inorganic solid-electrolyte interphase for stable lithium metal batteries under lean electrolyte conditions. Nat. Mater. *18*, 384–389.
28. Ryu, H.-H., Park, K.-J., Yoon, C.S., and Sun, Y.-K. (2018). Capacity fading of Ni-rich Li $[Ni_xCo_yMn_{1-x-y}]O_2$ $(0.6 \le x \le 0.95)$ cathodes for high-energy-density lithium-ion batteries: bulk or surface degradation? Chem. Mater. *30*, 1155–1163.
29. Sun, H.-H., and Manthiram, A. (2017). Impact of microcrack generation and surface degradation on a nickel-rich layered Li $[Ni_{0.9}Co_{0.05}Mn_{0.05}]O_2$ cathode for lithium-ion batteries. Chem. Mater. *29*, 8486–8493.
30. Li, H., Li, J., Ma, X., and Dahn, J.R. (2018). Synthesis of single crystal $LiNi_{0.6}Mn_{0.2}Co_{0.2}O_2$ with enhanced electrochemical performance for lithium ion batteries. J. Electrochem. Soc. *165*, A1038–A1045.
31. Jung, R., Linsenmann, F., Thomas, R., Wandt, J., Solchenbach, S., Maglia, F., Stinner, C., Tromp, M., and Gasteiger, H.A. (2019). Nickel, manganese, and cobalt dissolution from Ni-rich NMC and their effects on NMC622-graphite cells. J. Electrochem. Soc. *166*, A378–A389.
32. Shen, C.-H., Wang, Q., Chen, H.-J., Shi, C.-G., Zhang, H.-Y., Huang, L., Li, J.-T., and Sun, S.-G. (2016). In situ multitechnical investigation into capacity fading of high-voltage $LiNi_{0.5}Co_{0.2}Mn_{0.3}O_2$. ACS Appl. Mater. Interfaces *8*, 35323–35335.
33. Friedrich, F., Strehle, B., Freiberg, A.T.S., Kleiner, K., Day, S.J., Erk, C., Piana, M., and Gasteiger, H.A. (2019). Capacity fading mechanisms of NCM-811 cathodes in lithium-ion batteries studied by X-ray diffraction and other diagnostics. J. Electrochem. Soc. *166*, A3760–A3774.
34. Laszczynski, N., Solchenbach, S., Gasteiger, H.A., and Lucht, B.L. (2019). Understanding electrolyte decomposition of graphite/NCM811 cells at elevated operating voltage. J. Electrochem. Soc. *166*, A1853–A1859.
35. Yamada, Y., Wang, J., Ko, S., Watanabe, E., and Yamada, A. (2019). A. Advances and issues in developing salt-concentrated battery electrolytes. Nat. Energy *4*, 269–280.
36. Watanabe, M., Thomas, M.L., Zhang, S., Ueno, K., Yasuda, T., and Dokko, K. (2017). Application of ionic liquids to energy storage and conversion materials and devices. Chem. Rev. *117*, 7190–7239.
37. Kato, Y., Hori, S., Saito, T., Suzuki, K., Hirayama, M., Mitsui, A., Yonemura, M., Iba, H., and Kanno, R. (2016). High-power all-solid-state batteries using sulfide superionic conductors. Nat. Energy *1*, 16030.
38. Randau, S., Weber, D.A., Kötz, O., Koerver, R., Braun, P., Weber, A., Ivers-Tiffée, E., Adermann, T., Kulisch, J., Zeier, W.G., et al. (2020). Benchmarking the performance of all-solid-state lithium batteries. Nat. Energy *5*, 259–270.
39. Liu, J., Bao, Z., Cui, Y., Dufek, E.J., Goodenough, J.B., Khalifah, P., Li, Q., Liaw, B.Y., Liu, P., Manthiram, A., et al. (2019). Pathways for practical high-energy long-cycling lithium metal batteries. Nat. Energy *4*, 180–186.
40. Weber, R., Genovese, M., Louli, A.J., Hames, S., Martin, C., Hill, I.G., and Dahn, J.R. (2019). Long cycle life and dendrite-free lithium morphology in anode-free lithium pouch cells enabled by a dual-salt liquid electrolyte. Nat. Energy *4*, 683–689.
41. Chen, S., Zheng, J., Yu, L., Ren, X., Engelhard, M.H., Niu, C., Lee, H., Xu, W., Xiao, J., Liu, J., et al. (2018). High-efficiency lithium metal batteries with fire-retardant electrolytes. Joule *2*, 1548–1558.
42. Ko, M., Chae, S., Ma, J., Kim, N., Lee, H.-W., Cui, Y., and Cho, J. (2016). Scalable synthesis of silicon-nanolayer-embedded graphite for high-energy lithium-ion batteries. Nat. Energy *1*, 16113.
43. Zhu, Z., Yu, D., Yang, Y., Su, C., Huang, Y., Dong, Y., Waluyo, I., Wang, B., Hunt, A., Yao, X., et al. (2019). Gradient Li-rich oxide cathode particles immunized against oxygen release by a molten salt treatment. Nat. Energy *4*, 1049–1058.
44. Cui, C., Fan, X., Zhou, X., Chen, J., Wang, Q., Ma, L., Yang, C., Hu, E., Yang, X.-Q., and Wang, C. (2020). Structure and interface design enable stable Li-rich cathode. J. Am. Chem. Soc. *142*, 8918–8927.
45. Pieczonka, N.P.W., Liu, Z., Lu, P., Olson, K.L., Moote, J., Powell, B.R., and Kim, J.-H. (2013). Understanding transition-metal dissolution behavior in $LiNi_{0.5}Mn_{1.5}O_4$ high-voltage spinel for lithium ion batteries. J. Phys. Chem. C *117*, 15947–15957.